Geophys. J. Int. (2006) **164,** 202–217 doi: 10.1111/j.1365-246X.2005.02655.x

The 1994 Sefidabeh (eastern Iran) earthquakes revisited: new evidence from satellite radar interferometry and carbonate dating about the growth of an active fold above a blind thrust fault

B. Parsons,[1] T. Wright,[1] P. Rowe,[2] J. Andrews,[2] J. Jackson,[3] R. Walker,[3] M. Khatib,[4] M. Talebian,[5] E. Bergman[6] and E. R. Engdahl[6]

[1] *COMET, Department of Earth Sciences, University of Oxford, Oxford* OX1 3PR, *UK. E-mail: barry.parsons@earth.ox.ac.uk*
[2] *School of Environmental Sciences, University of East Anglia, Norwich,* NR4 7TJ, *UK*
[3] *COMET, Bullard Laboratories, University of Cambridge, Cambridge* CB3 0EZ, *UK*
[4] *Department of Geology, University of Birjand, Birjand, Iran*
[5] *Geological Survey of Iran,* PO Box 13185-1494, *Tehran, Iran*
[6] *CIEI, Department of Physics, University of Colorado, Boulder,* CO 80309, *USA*

Accepted 2005 April 7. Received 2005 February 28; in original form 2004 May 4

SUMMARY

In 1994, three shallow earthquakes of $M_w \sim 6$ occurred close together on blind thrusts near Sefidabeh in eastern Iran. In an earlier study of the teleseismic waveforms, the geomorphology and the faulting in the epicentral region, it was suggested that these earthquakes were associated with the growth of a ridge above a blind thrust fault system, whose activity could be detected by its effect on the surface drainage. In this study we present a SAR interferogram that precisely determines the location and amount of coseismic surface displacements, showing that the earthquakes in the Sefidabeh sequence probably occurred on en-echelon fault segments associated with three stepping ridges. We also present U/Th dates of ∼100 ka for lake deposits uplifted by the growing ridge. From the cumulative, dated uplift and knowledge of the surface displacements due to an earthquake sequence, we estimate that ∼120 such events have occurred in the past 100 ka, with an average recurrence interval of 830 yr, and an average convergence rate of 1.5 mm yr^{-1} on the Sefidabeh thrust; each estimate has an uncertainty of a factor of two, either way. We argue that the Sefidabeh fault originally formed by coalescence of many small fault segments, and has grown in length at about 2 cm yr^{-1} in the past 100 ka. Though the coseismic surface deformation observed in the SAR interferogram closely resembles folding, the overall topography does not, because of inherited topography associated with earlier geological deformation. In spite of this, the activity of the buried thrust fault can easily be detected by its effect on the surface drainage: a significant lesson when interpreting landscapes that are not entirely due to the present-day deformation.

Key words: continental deformation, earthquakes, geochronology, Iran, SAR interferometry.

1 INTRODUCTION

The topography of tectonically active areas reflects the tectonic processes at work. In particular, the topography associated with active faults must ultimately be due to the cumulative effect of the uplift and subsidence occurring in individual earthquakes. However, if the only information available is the present-day topography itself, then the connection between earthquake deformation and present topography can be made only by assuming the likely deformation due to a single earthquake. Without independent information about the age of the topographic features, nothing can be said about the rates of processes that have created the present landscape.

In this paper, we show how additional information from geodesy and modern dating methods can remove many of these uncertainties, by taking a new look at a sequence of four earthquakes, with magnitudes (M_W) 5.5–6.2, that occurred within a few days of each other in 1994 February near the village of Sefidabeh in eastern Iran. The initial study by Berberian *et al.* (2000) of these earthquakes was based on field observations, satellite imagery and seismology, and suggested that the fault system responsible involved blind faulting beneath a NW–SE trending ridge southwest of, and adjacent to the village of Sefidabeh itself (Figs 1–4). Since that study, new information has come from two main sources. First, we have been able to obtain a synthetic aperture radar (SAR) interferogram,

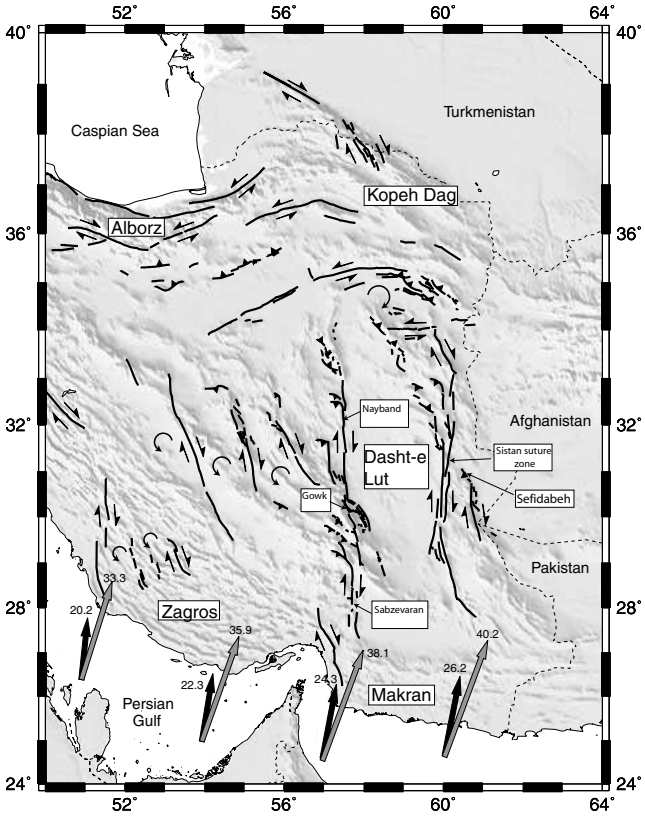

Figure 1. Major fault zones and geographical regions of central and eastern Iran, superimposed on a GTOPO30 image of the area. Black and grey arrows are estimates of Arabia–Eurasia plate motions, with rates in mm yr^{-1}. Black arrows are GPS estimates (Sella *et al.* 2002); grey arrows are derived from Africa–Arabia (DeMets *et al.* 1994) and Africa–Eurasia (Chu & Gordon 1998) plate motions based on rates from 3 Ma marine magnetic anomalies. Arabia–Eurasia convergence is taken up in the Zagros, the Alborz and Kopeh Dagh, and possibly in central Iran by rotation of strike-slip faults. Right-lateral shear between central Iran and Afghanistan is taken up on N–S right-lateral faults of the Nayband–Gowk–Sabzevaran and Sistan Suture Zone systems on the west and east sides of the Dasht-e-Lut. Sefidabeh lies in the Sistan fault belt.

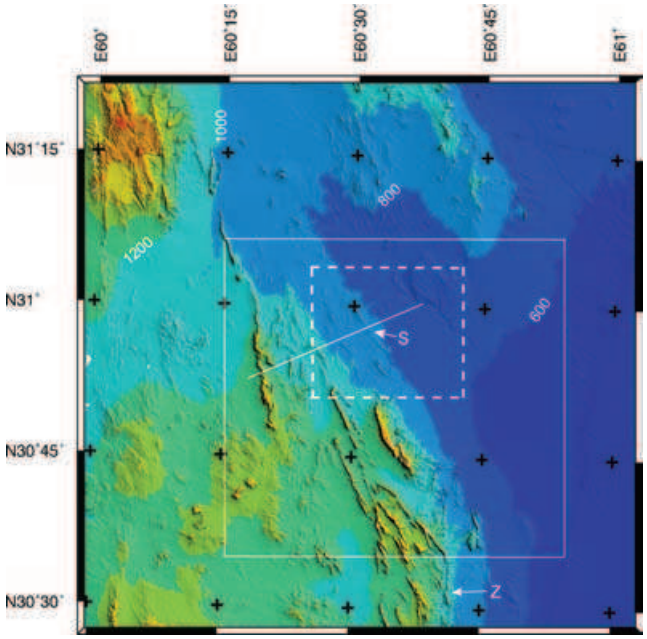

Figure 2. Coloured shaded relief map for the Sistan fault belt centred on Sefidabeh, based on a 40 m posting DEM made using InSAR and an ERS tandem pair with gaps infilled using 90 STRM data as described in Section 3.1. The topography is colour contoured every 200 m, and the topography is illuminated from an azimuth of 58° and an elevation of 50°. S is Sefidabeh and Z is the Zahedan fault. The line shows the location of the topographic profile shown in Fig. 3. The box with dashed borders shows the extent of the Landsat image and shaded relief map in Fig. 4. The box with the solid border shows the extent of the SAR interferogram and model calculations in Fig. 6 and subsequent figures.

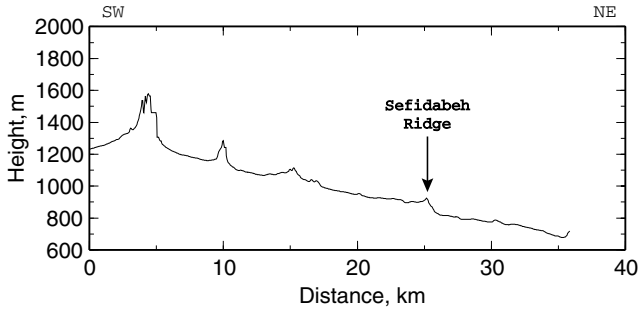

Figure 3. Topographic profile from the 40 m posting DEM along the line shown in Fig. 2.

showing that the surface displacements that occurred in the earthquakes produced a relatively simple pattern of folding above buried thrust faults. Second, it has been possible to date now-uplifted deposits, which together with the observed surface displacements, allows the number and frequency of past earthquakes to be estimated directly, as well as the slip rate on the faults. As with the clear geomorphological features in the area, the preservation of the dateable deposits and the quality of the interferometry owe much to its location in the desert climate of eastern Iran.

2 THE LOCATION AND SETTING OF THE SEFIDABEH EARTHQUAKES

2.1 Active tectonics

The Sefidabeh area lies within the Sistan fault belt, the eastern of two fault belts located on each side of the flat, low-lying and aseismic Lut desert (Fig. 1). Together these two fault systems accommodate 13–16 mm yr^{-1} of right-lateral shear between central Iran and Afghanistan, with the Sistan fault system taking up about 10–13 mm yr^{-1} (Walker & Jackson 2002, 2004; Vernant *et al.* 2004). The motion between central Iran and Afghanistan, part of the Eurasian plate, arises because the ∼25 mm yr^{-1} of convergence between the Arabian and Eurasian plates is accommodated both in the Zagros mountains in SW Iran and in the Alborz and Kopeh Dagh in northern Iran.

In the part of the Sistan belt where Sefidabeh lies, the principal active structures are large N- to NNE-striking right-lateral strike-slip faults such as the Zahedan and East and West Neh faults. There are in addition NW-striking thrusts, many being located at the ends of the strike-slip faults. The Sefidabeh blind thrust is one such thrust that, together with the neighbouring Palang Kuh thrust, terminates the northern end of the Zahedan strike-slip fault. It is believed that the role of thrust faults in terminating major strike-slip faults is to

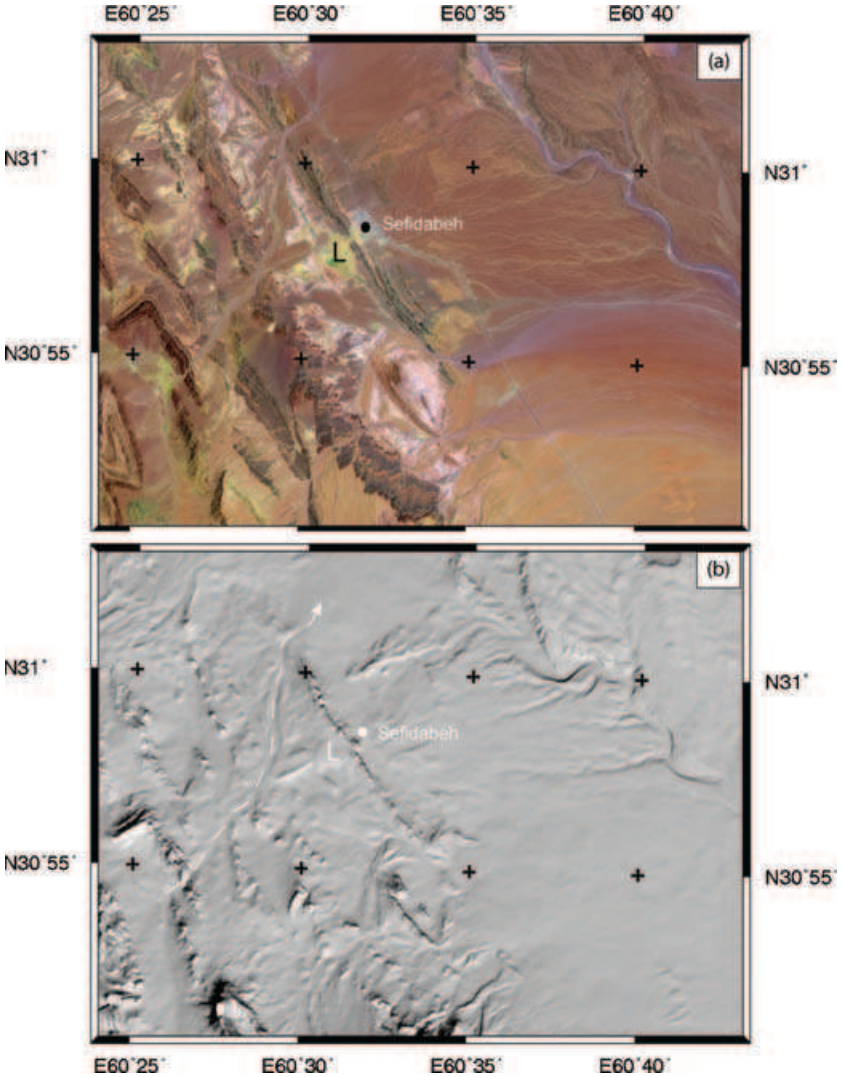

Figure 4. (a) Landsat-7 ETM imagery for the area of Sefidabeh. The image is a false colour composite using band 7 (red), band 4 (green) and band 1 (blue) from a mosaic of ETM images recorded on 2001/06/25 (158/38) and 2001/05/8 (158/39). The uplifted lake deposits are marked with L. (b) Shaded relief for the same area from the InSAR DEM derived in this study. The illumination is from an azimuth of 148°E, that is, parallel to the local ridges, and an elevation of 40°. The banks of the deflected Butgow river (dashed white line) may be seen cutting across the pre-existing river that used to drain directly downslope and later supplied the now-uplifted lake.

enable structural rotations about a vertical axis (Bayasgalan *et al.* 1999; Berberian *et al.* 2000).

2.2 Topography and drainage

In exploring the topography and drainage of the Sefidabeh area, we have made use of a 40-m-resolution digital elevation model (DEM; Fig. 2), the construction of which is described below in the section on InSAR analysis. The Sefidabeh ridge, which rises just over 100 m above the plain beneath it, is superimposed on a regional slope of about 600 m in 30 km (Fig. 3).

Features in the drainage around the Sefidabeh ridge may be highlighted in shaded relief maps with the appropriate direction of illumination (Fig. 4b). In particular, a substantial river, the Rud-e-Butgow, appears to be deflected round the northern end of the ridge. Berberian *et al.* (2000) suggested that prior to the growth of the NW–SE ridge the drainage was directly down the regional slope. As the ridge grew in repeated earthquakes across the path of the river, defeating the river in its attempt to cut through the ridge, a lake formed. Subsequently the river was deflected and the lake drained, leaving the light-coloured deposits that can be seen in the Landsat-7 ETM image in Fig. 4(a). It is these deposits, which are now found ∼70 m above the Sefidabeh plain, that we sampled and subjected to U-series dating, in order to constrain the age at which the lake deposits ceased to form, and began to be uplifted.

2.3 Earthquake locations

The published teleseismic epicentres of the five main earthquakes in the 1994 Sefidabeh sequence are very close together (Fig. 5; Berberian *et al.* 2000). In an attempt to see whether we could resolve any difference in position between them, we carried out multiple event relocation on the sequence using the hypocentroidal decomposition (HDC) method (Jordan & Sverdrup 1981). The basic method has been updated with modern earthquake location algorithms and data set from the EHB single event algorithm

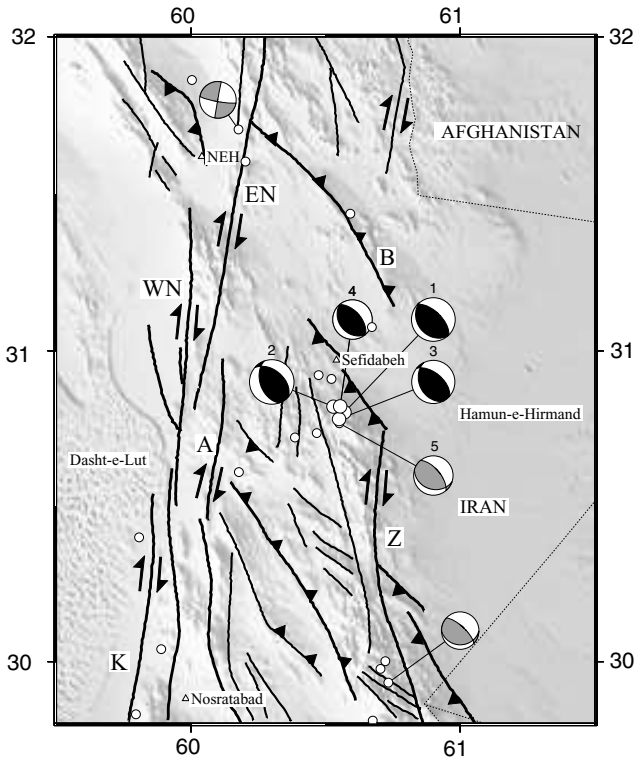

Figure 5. Faulting and focal mechanisms in the Sistan suture zone. Large white circles and accompanying black-shaded focal spheres are the published locations and mechanisms of the four main earthquakes (1–4) in the Sefidabeh sequence for which Berberian *et al.* (2000) carried out body-wave modelling. Grey focal spheres are Harvard CMT solutions. Events 1–5 are numbered as in Table 1. Small white circles are earthquakes in the period 1964–1998 located by Engdahl *et al.* (1998). Faults: A, Asagi fault; B, Banan fault; EN & WN, East and West Neh faults; K, Kahurak fault; Z, Zahedan fault.

(Engdahl *et al.* 1998), and further developed and tested through generating and validating 'ground truth' data sets (e.g. Ritzwoller *et al.* 2003; Bondar *et al.* 2004) for regional and teleseismic location studies.

The HDC method naturally separates the problem into two parts:

(1) estimation of locations and times, the so-called 'cluster vectors', relative to the current geometric centroid (the 'hypocentroid') of the cluster and

(2) estimation of location and origin time of the hypocentroid in geographic coordinates and UT. This establishes the absolute coordinates and origin times for all the cluster events, by adding the relative cluster vectors to the hypocentroid. The HDC algorithm is notable for making full use of all information contained in the data set on relative locations. It also provides a rigorous treatment of the error budget. Reliable error estimates are made through estimation of reading errors for each station–phase combination, which is based in turn on analysis of the residual statistics of earlier runs.

The relocation of the Sefidabeh cluster was complicated by one event, 940226.0231, which initially had unusually large traveltime residuals. Analysis of the data indicated a bimodal distribution of readings consistent with a multiple source. This can also be seen in body waveform inversion of Berberian *et al.* (2000; Fig. 8) for this event, which shows a source time function with a small precursory pulse followed several seconds later by a large pulse of energy. For the relocation, we have screened the data set to remove most of the readings associated with the initial, smaller pulse of energy.

The locations with their uncertainties are given in Table 1. Depths were initially fixed at 9 km, the mean depth of the events looked at by Berberian *et al.* (2000). The depths of two events whose locations were found to be northeast, updip for the faults discussed in Section 3.2, were set to 7 km. The absolute locations of the cluster are subject to systematic bias; the magnitude and direction of this bias may be estimated by comparison of the seismic location with the geodetic location determined by modelling with a SAR interferogram. We return to this point in Section 3.2. The relative locations of the individual events are spread over about 10 km, a length that is significant compared with the estimated errors in the locations. As we show below in 3.2, where we develop a three-fault model to explain the observed SAR interferogram, the spread of event locations in the Sefidabeh sequence locations is comparable to the distance over which slip on the faults extends.

3 SURFACE DISPLACEMENTS FROM INSAR

3.1 InSAR analysis

The phase differences in complex SAR images of the ground taken before and after an earthquake can be used to make an interferogram that gives the component of the surface displacement in the line of sight to the satellite (e.g. Massonnet & Feigl 1998). Each fringe represents half-a-wavelength of displacement of the surface towards or away from the satellite, which in the case of ERS-1/ERS-2 is 28 mm. The line-of-sight displacements may be determined to subcentimetric precision with a dense spatial sampling. In addition, InSAR may be used to construct high-resolution DEMs.

To start, we constructed a DEM of the Sefidabeh area using an ERS-1/ERS-2 tandem pair (Table 2). The time interval between acquisitions by ERS-1 and then ERS-2 in an ERS tandem pair is 1 day, keeping changes in the scattering properties of the ground to a minimum. The altitude of ambiguity for the chosen tandem pair—the change in elevation that produces a 2π or 360° phase change

Table 1. Locations for the Sefidabeh earthquake sequence determined with the HDC method. Numbers in parentheses after the date identify the five numbered events in Fig. 5. Locations relative to the first earthquake on 1994 February 23 at 080204GMT are given in km (Δx, E; Δy, N). Magnitudes are M_w except for those marked by $*$ which is m_b. Seismic moments (M_0) are in units of 10^{18} N m. σ_a and σ_b are, respectively, the lengths of the major and minor axes of the error ellipse; θ_a° is the azimuth of the major axis of the error ellipse measured clockwise from north.

Date	Time	Lat.	Long.	Depth	M_w	M_0	Δx (km)	Δy (km)	σ_a (km)	θ_a°	σ_b (km)
1994/02/23 (1)	08:02:06.24	30.870	60.520	7	6.1	1.5			1.3	13	0.6
1994/02/23 (5)	11:54:34.27	30.837	60.510	9	5.5	0.2	−0.6	−3.7	1.6	9	0.8
1994/02/23	22:45:19.23	30.902	60.470	9	5.4*		−2.8	3.6	1.7	8	0.8
1994/02/24 (2)	00:11:13.77	30.881	60.473	9	6.2	2.5	−2.6	1.2	1.4	13	0.6
1994/02/26 (3)	02:31:12.53	30.817	60.530	9	6.0	1.1	0.6	−5.9	1.8	12	0.8
1994/02/28 (4)	11:13:55.25	30.884	60.527	7	5.5	0.2	0.4	1.6	1.5	10	0.6

Table 2. ERS SAR data used in the InSAR analysis.

	Date 1	Orbit 1[a]	Date 2	Orbit 2[a]	$B_\perp$[b]	h_a[c]
(1) DEM generation	1996/05/04	25115 (ERS-1)	1996/05/05	5442 (ERS-2)	104	87
(2) Coseismic pair	1993/01/07	7737 (ERS-1)	1996/03/31	4941 (ERS-2)	29	353

[a]Track 77, frame 2985; ERS SAR data © European Space Agency.
[b]$B_\perp$ is the perpendicular baseline, that is, the component of the orbital separation perpendicular to the line of sight from satellite to the ground.
[c]h_a is the altitude of ambiguity.

in an interferogram—is 87 m. We constructed a SAR interferogram with the tandem pair, and transformed that to a ground registered DEM with a posting of 40 m, using the JPL/Caltech ROI_pac software (Rosen *et al.* 2004). In calibrating the orbital baseline between satellite passes, and in removing residual biases and tilts, the 1 km posting GTOPO30 DEM was used.

Recently a Shuttle Radar Topographic Mission (SRTM) DEM (Farr & Kobrich 2000) was released for this area. The 40-m InSAR DEM and 90-m SRTM DEM agree quite well, apart from a small translation error. The two were matched, and the SRTM topography used to fill in holes in the InSAR DEM. Topography from the resulting DEM is shown above in Fig. 2; quite subtle and coherent features may be observed in shaded-relief maps made from it (e.g. Fig. 4b, Fig. 6). Note, in particular, that the NW–SE ridge next to Sefidabeh is the northern one of a series of en-echelon, right-stepping ridges extending over a distance of about 30 km. Given the arid nature of the area, path differences and hence topographic errors due to tropospheric water vapour are likely to be small. Differences between the InSAR DEM constructed here and SRTM heights have a standard deviation of about 7 m, about the error expected for SRTM alone, suggesting that the errors in the InSAR DEM are probably smaller than those in the SRTM data.

The coseismic interferogram (Fig. 6) was also constructed using the JPL/Caltech ROI_pac software. The topographic corrections were made with the 40-m InSAR DEM; with an altitude of ambiguity of 353 m, range errors due any topographic errors will be ∼1 mm. The time interval between ERS SAR acquisitions before and after the Sefidabeh earthquakes is slightly longer than 3 years (Table 2). Nonetheless, for the most part the coherence is very high, probably the result of the arid environment and the consequently low rates of surface alteration. The main area of low coherence—the gap on the eastern side of the dominant set of fringes in Fig. 6—is over the Sefidabeh ridge and the en-echelon ridges to the south. A likely reason for this is the bedding-plane slip on near vertical beds

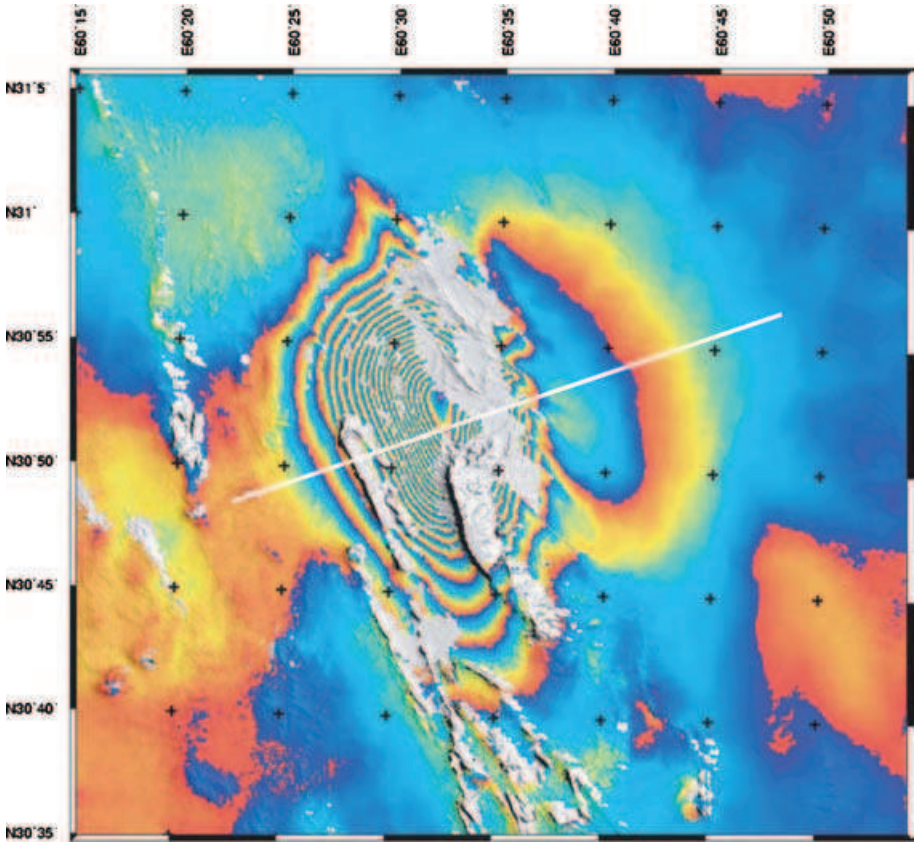

Figure 6. Coseismic interferogram for the epicentral area of the 1994 Sefidabeh earthquakes. This overlies topography as shaded relief derived from the infilled InSAR DEM, which can be seen directly in areas of poor coherence masked in the interferogram. Each colour cycle from blue to red represents an increase of 28 mm in the range to the satellite. The line gives the location of the profile of unwrapped phase shown in the next figure. This figure and those for the model calculations use a Universal Transverse Mercator projection, zone 41.

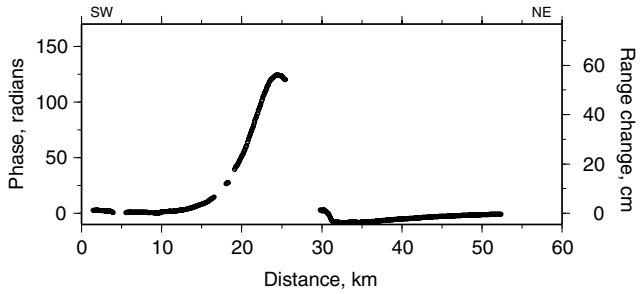

Figure 7. Phase variations and range changes along the profile shown in Fig. 6. A phase change of 2π is equivalent to a line-of-sight range change of 28.3 mm. We have chosen a sign convention chosen here so that movement towards the satellite (range decrease) corresponds to positive phase.

observed by Berberian *et al.* (2000), which results locally in large displacement gradients and a disturbed surface.

The interferogram is mainly smoothly varying on a length scale of about 15 km perpendicular to the ridges (Fig. 6). It shows the asymmetry typical of a steeply dipping thrust fault between larger hanging wall uplift in the west and smaller footwall subsidence to the east, an asymmetry in the opposite sense to that observed in normal fault earthquakes (e.g. Wright *et al.* 1999). In the area of subsidence closest to the topographic ridges, the fringes show an en-echelon effect, suggesting separate contributions from slip associated with each of the ridges. A profile of unwrapped phase across the interferogram gives a maximum phase change of about 125 radians, equivalent to about 0.55 m of displacement towards the spacecraft (Fig. 7). If we assume that most of the motion is vertical at the maximum, this corresponds to 0.6 m of uplift. It should be noted that the surface displacements revealed by the coseismic interferogram represent the net deformation of all the events making up the sequence of earthquakes at Sefidabeh. Nonetheless, this magnitude of uplift is of the order expected for earthquakes with $M_w \sim 6.0$, with about 1 m of slip in each event (Berberian *et al.* 2000). Note also that the wavelength of the uplift, ∼10–15 km, is that expected for reverse faulting in a seismogenic layer 10–15 km thick.

3.2 Modelling of fault plane slip

The interferogram we have derived has phase changes or equivalent line-of-sight surface displacements on an 80 m grid, producing too many values to be easily assimilated in a rapid inversion scheme. In order to reduce the number of data values to be used, we subsample the interferogram using the quadtree method (e.g. Jónsson *et al.* 2002). The mean value of the phase in a block, assumed located at its centre, is used in the modelling if the variance of phase values in the block is less than the noise variance estimated from part of the interferogram away from the coseismic fringes. Otherwise, the block is subdivided into four equal parts and the test repeated. A maximum block size of 7 km was chosen, equal to the length scale of the covariance function of the phase (see Appendix A), again calculated using part of the interferogram away from the coseismic fringes. The number of phase samples was reduced in this way to 1512 from $\sim 3 \times 10^6$ in the full interferogram.

3.2.1 Slip on a single fault plane

An initial attempt was made to model the net displacements produced by the Sefidabeh earthquakes as those due to uniform slip on a single rectangular fault plane, following the approach of Wright *et al.* (1999). The surface displacement vector (**u**) at each point produced by the elastic dislocation was calculated using the expressions given by Okada (1985), and then projected into the satellite line of sight ($\Delta l = -\hat{\mathbf{n}} \cdot \mathbf{u}$), using the unit vector ($\hat{\mathbf{n}}$) pointing to the satellite calculated locally at each observation location. A non-linear, downhill simplex algorithm, with Monte Carlo restarts to avoid local mimina, was used to determine nine fault parameters (Table 3) plus a line-of-sight offset. Formal errors on the fault parameters were obtained as described in Appendix A.

The best-fitting solution with uniform slip on a single fault (column 1, Table 3) fails to predict a number of features, for example, the tapering of the fringes at the south and the angular fringes at the north (Fig. 8a), and consequently there are a number of significant residuals (Fig. 8b). The strike of the fault (161°) is greater than that of each of the en-echelon ridges (148°), but rather represents the average strike of the system of ridges. This suggests that slip may have occurred separately on separate faults related to the ridges, and the uniform single fault model compensates for this by rotating its strike.

To investigate this further, we sought another solution with uniform slip on a single fault where the strike was fixed at that of the ridges (column 2, Table 3). We then extended the length of this fault to 25 km, and from the surface to a depth of 20 km, and solved for distributed slip on this plane with its geometry fixed to that of the

Table 3. Fault parameters for single fault, uniform slip calculations. Eastings and northings are in UTM zone 41, and represent the centre of the line where the fault plane would intersect the surface if extended. Errors (see Appendix A2) are 1 standard deviation rounded to last decimal place. Because of the constrained nature of the three-fault solution, error estimates were not made in this case.

	One fault		Three faults		
	Free strike	Fixed strike	1	2	3
Strike	161 ± 1	148	148	148	148
Dip	47 ± 1	46 ± 1	45	45	45
Rake	89 ± 3	68 ± 2	105	105	105
Slip (m)	1.95 ± 0.07	1.78 ± 0.05	1.5	1.5	0.75
Length (km)	12.7 ± 0.1	12.0 ± 0.1	5	7.5	8
Min depth (km)	4.4 ± 0.1	4.0 ± 0.1	5	2.8	4.4
Max depth (km)	10.1 ± 0.2	10.2 ± 0.2	11.7	9.5	9.7
Easting (km)	269.6 ± 0.1	268.2 ± 0.1	269.2	268.3	270.6
Northing (km)	3420.0 ± 0.2	3422.3 ± 0.1	3426.5	3419.8	3412.6
$M_0 \times 10^{18}$ Nm	6.6 ± 0.1	6.4 ± 0.1	2.4	3.6	1.5
				Total = 7.5	
M_w	6.5	6.5	6.2	6.3	6.1

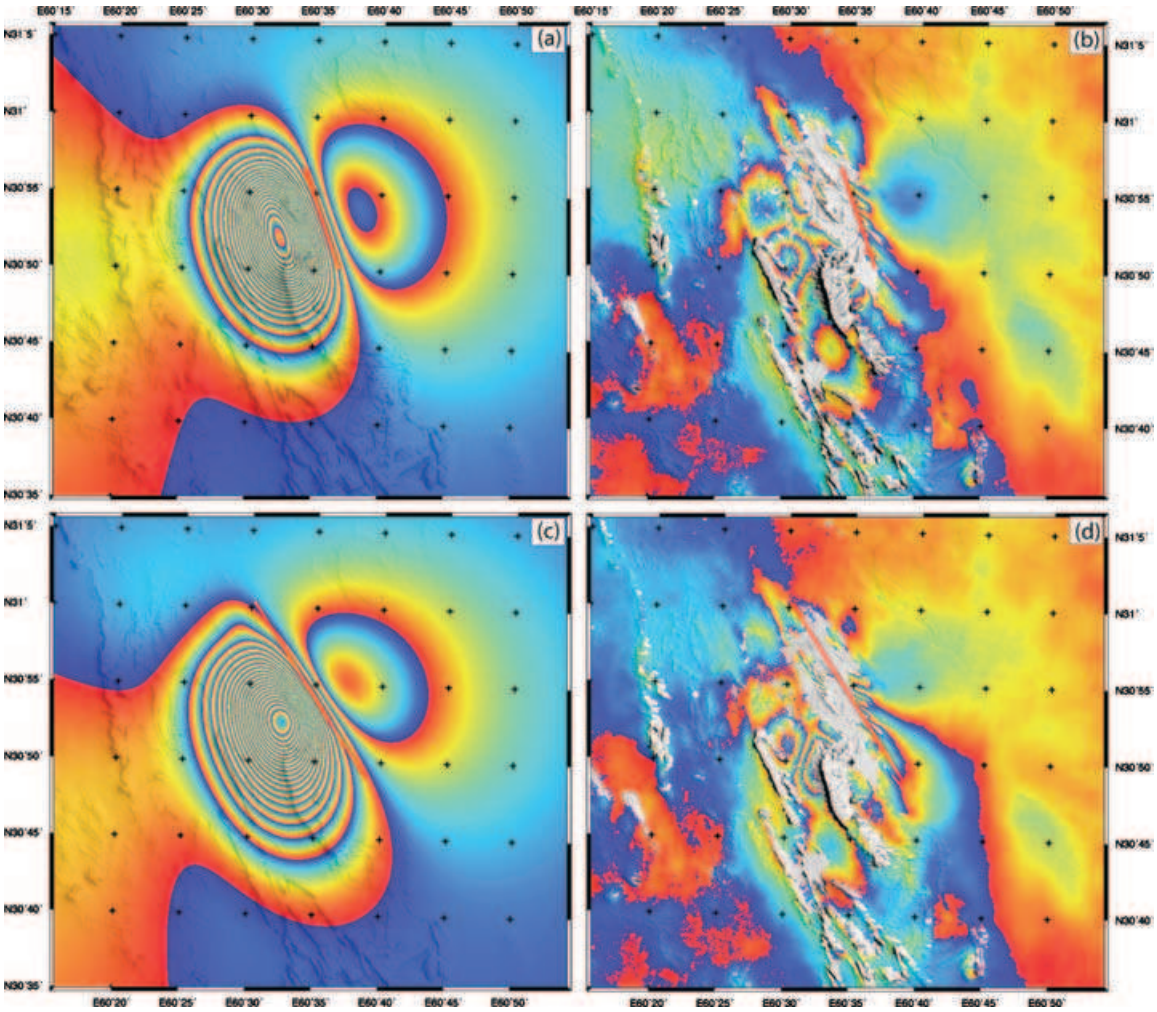

Figure 8. Model interferograms and residuals for calculations with slip on a single fault. Each colour cycle represents 28 mm of range change. The red lines show where the fault plane, if extended, would intersect the surface. (a) Model interferogram with uniform slip on fault (see Table 3). (b) Residual (observed minus model) fringes for uniform slip calculation. (c) Model interferogram with distributed slip on extended fault plane. (d) Residual fringes for the distributed slip calculation.

fixed-strike, uniform-slip solution. The method used to obtain the distribution of slip is described in Wright *et al.* (2004). The fault surface was divided into 80 patches, each 2.5 km long and 2.5 km high, the line-of-sight surface displacements due to slip on each patch being calculated using the expressions of Okada (1985) as before. To prevent unphysical oscillatory slip or retrograde motion on the fault, Laplacian smoothing was imposed. There is a trade-off between the roughness and the rms misfit of the solution; the weighting of the Laplacian smoothing was chosen to give a solution that had both low misfit and roughness (Wright *et al.* 2004). Errors for this non-linear inversion were determined using the method described in Appendix A.

The resulting slip distribution is given in Fig. 9, with the predicted line-of-sight displacements and the corresponding residuals shown in Figs 8(c) and (d). The interferogram does a better job at predicting the shape of the fringes in the north, but there are still some significant residuals at the southern end of the faulting, where the model interferograms seem too rounded.

3.2.2 Slip on three fault planes

The surface displacements are actually the combined effect of similar earthquakes located close to each other. The limitations to how well we could reproduce the interferogram with slip on a single fault, and the features of these solutions, suggests that the slip occurred on more than one fault plane, possibly associated with the different ridge segments seen in the topography. We, therefore, decided to try to find a model with slip on three fault planes, as three of the events in the 1994 Sefidabeh sequence are larger than the others (Table 1; Berberian *et al.* 2000).

The lengths of the fault segments were estimated from the ridge segments in the topography, constrained by the location of the ends of the fault in the single fault solution. Guided by the single fault solutions and the seismic source mechanisms of Berberian *et al.* (2000), the strike (148°), dip (45°), rake (105°), and slip (1.5 m) were then all fixed, and we then solved for minimum and maximum depth of faulting and location of each segment. This solution was further refined by fixing everything apart from the slip and depth extents on the southern segment (Table 3). Given the highly constrained nature of this calculation, we did not attempt a formal error analysis.

The total moment we obtain (Table 3) is about 40 per cent larger than the combined seismic moment, perhaps not surprising considering the long time interval spanned by the interferogram. The relative moments we calculated for each of the segments are very

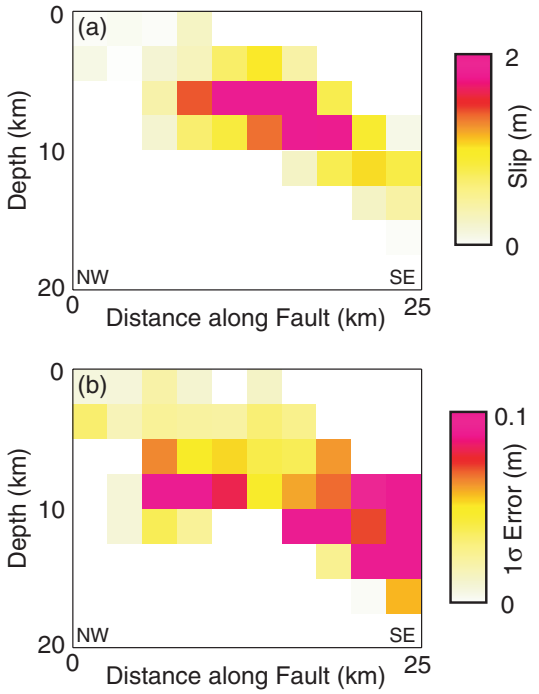

Figure 9. (a) Slip and (b) associated errors for distributed slip on a single fault. The model interferogram and residual fringes calculated with this slip distribution are shown in Figs 8(c) and (d).

similar to those determined seismologically for the separate events (Table 1; Berberian *et al.* 2000), and the centres of the individual fault segments are similar in depth to the centroids determined seismologically, which are all in the range 5–10 km (±4 km). The predicted and residual solutions for this source model are shown in Fig. 10. The shape of the southern part of the interferogram is improved, but the angular northern feature is not well represented. There are still significant residuals, largely at the offsets between segments.

We then extended the length of the northern segment to the north, and the length of the southern segment to the south, and extended all segments in depth. A variable distribution of slip was then sought on each fault segment as before, the faults being divided into a total of 144 patches, with dimensions of 2.5 km in length and 2.5 km in depth as before (Fig. 11). The interferogram is now reasonably well reproduced, the residuals generally being small and randomly distributed (Figs 10c and d).

The modelling is obviously highly non-unique. Nonetheless, we feel it is a reasonable hypothesis, based on the above calculations, that the earthquakes in the Sefidabeh sequence occurred on separate fault segments. As discussed in Section 2.3, although we know the relative locations of the Sefidabeh earthquakes events well, the absolute location of the cluster is subject to bias. The centre of the cluster lies about 10.4 km away on an azimuth of 170° from the centre of the area of significant fault slip. If we remove this bias by shifting the cluster by 10.4 km in the opposite direction, we can see that the extent of the area of maximum slip in Fig. 11 compares well with the spread of earthquake locations. We also note that the regions of maximum slip on the fault segments in Fig. 11 appear to be aligned, suggesting that slip on one segment may then have triggered slip on its neighbour.

4 PETROGRAPHIC AND ISOTOPE ANALYSIS OF THE SEFIDABEH CARBONATES

The carbonates that are preserved in the now-abandoned and uplifted gorge near the village of Sefidabeh potentially contain information about the chronological and climatic history of the uplifted ridge and its drainage system. Understanding the climatic history is important, if we are to exploit signals in the landscape related to the evolution of drainage patterns for tectonic purposes. We took six samples from a prominent bluff exposed at the top of the carbonate section, overlooking Sefidabeh (Fig. 12). Details of the petrography and isotope analysis are given in Appendix B. Only a summary of the pertinent results are given here in the main text.

The deposit, wrongly identified as a travertine by Berberian *et al.* (2000), is essentially a calcite-cemented sandstone, which in its upper part has been almost totally cemented or replaced by non-ferroan early diagenetic calcite. These calcites contain petrographic evidence of microbial activity and at least three cement stages including some dripstone fabrics indicative of vadose zone conditions (i.e. above the water table) at times. Numerous vugs or fenestrae are common and these are now partially cemented. Some of the vugs may have contained evaporite salts, now dissolved. The environment of deposition seems to have been a sandy fluvial system draining a playa lake. Calcite formation either happened when surface drainage waters dried out, or more likely occurred in and around groundwater-fed springs, where carbonate formation is encouraged by degassing of dissolved CO_2. Upward-flowing groundwater caused rupturing of cemented crusts and development of fenestrae. Similar fenestral limestones, but with extensive aragonite cementation in this case, are known from semi-arid carbonate flats in south Australia (Ferguson *et al.* 1982). Overall, calcite cementation clearly occurred in conditions that were wetter than today, presumably as spring-fed drainage from the now-abandoned playa. Moreover, the petrographic evidence of well-preserved non-ferroan early diagenetic fabrics imply that the carbonates have been unaffected by later diagenetic alteration and are unlikely to have undergone extensive isotopic exchange.

A high priority was to estimate the depositional age of the carbonates. The uranium–thorium technique is well established as a reliable method for dating a wide variety of Mid-Late Pleistocene secondary carbonates (Schwarcz 1989; Ivanovich & Harmon 1992). It depends on the ingrowth of ^{230}Th from ^{234}U decay, a process which takes 400–500 ka to reach equilibrium. Thus the relative activity of ingrown ^{230}Th gives a direct measurement of sample age. Necessary pre-conditions are that the carbonate should (a) initially contain no ^{230}Th and (b) remain an isotopically closed system.

However, in common with many subaerial carbonates, the Sefidabeh calcite cement incorporates thorium- and uranium-bearing siliciclastic detrital material in the form of sand, silt and clay, thus violating pre-condition (a) above. Such deposits (often referred to as 'dirty calcites') require more intensive U- and Th-isotopic study in order to determine an age. One common approach is to analyse several coeval subsamples, containing varying concentrations of the detrital contaminant, to recover isotopic data, which can then be plotted in U-Th isotope ratio space. Such plots define mixing lines (isochrons) between the pure calcite and pure detritus end members. The slopes or intercepts can be used to calculate sample age, depending on the isotope pairs plotted. This approach has been discussed in detail by Ku & Liang (1984), Schwarcz & Latham

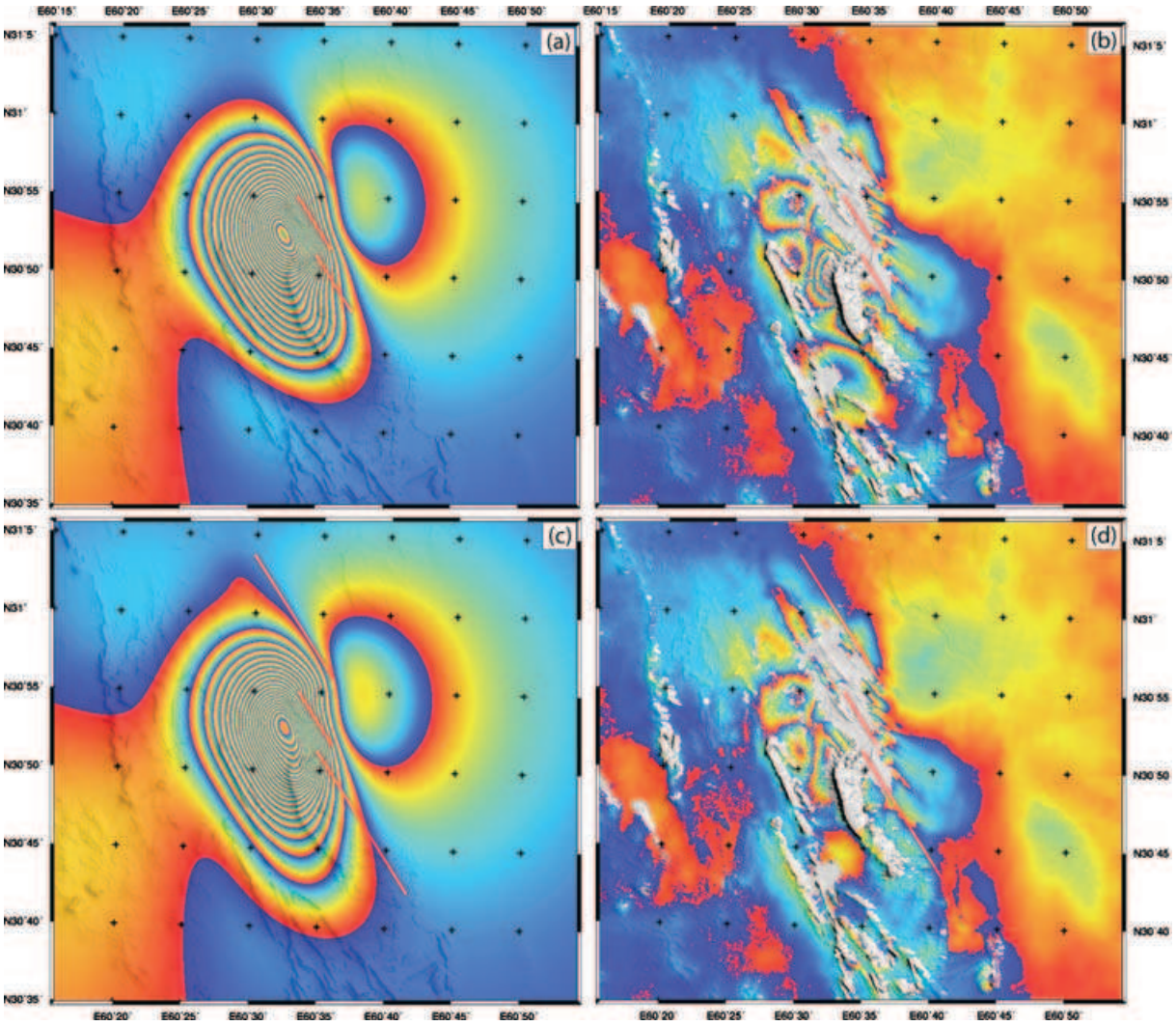

Figure 10. Model interferograms and residuals for calculations with slip on three en-echelon faults. The red lines show where the fault planes, if extended, would intersect the surface. (a) Model interferogram with uniform slip on faults (see Table 3). (b) Residual (observed minus model) fringes for uniform slip calculation. (c) Model interferogram for distributed slip with northern and southern fault planes extended. (d) Residual fringes for the distributed slip calculation.

(1989), Bischoff & Fitzpatrick (1991) and Luo & Ku (1991) and partially reviewed by Kaufman (1993). Ludwig & Titterington (1994) and Ludwig (2003) have discussed the statistical treatment of the sample data. Wide variation in contaminant concentration between subsamples is advantageous because this increases the prospect of obtaining a wide dispersion of isotopic ratios and hence better isochron definition. Commonly, however, detrital distribution within a carbonate deposit is rather homogenous, resulting in a compression of the isotopic data range that, when combined with analytical scatter, weakens isochron linearity. The samples analysed here were collected from a single locality within the tufa and the insoluble detrital content of the samples lay within the rather narrow range of 9–16 per cent.

The dating results are detailed in Appendix B2. Plotting ^{230}Th/^{232}Th versus ^{234}U/^{232}Th, five of the six data points lie within one standard deviation of the best-fit isochron, whilst one falls almost two standard deviations below the line. This contrasts with the ^{234}U/^{232}Th versus ^{238}U/^{232}Th isochron, where all six points lie very close to the fitted line. There is no incontrovertible *a priori* reason for rejecting this outlying point (although see Appendix B2) but, because it is highly influential, in constructing a six-point isochron we have used a robust, non-parametric regression algorithm of Ludwig (2001). This makes no assumptions about the causes of the observed data scatter and reduces the weighting given to such outliers. Based on the slope of the isochrons, the age of the Sefidabeh deposit is calculated to be 103^{+164}_{-57} ka (Table B2). Omitting the outlying datum, five-point isochrons yield an age of 99^{+30}_{-24} ka (Figures B1 and B2, Table B2).

These age estimates are sufficiently good to allow us to make quantitative estimates of likely fault growth rates and earthquake recurrence times, which are discussed in Section 5. However, the uncertainty in age has significance for climatic interpretations. The stable oxygen isotopic composition of the Sefidabeh calcite (Appendix B3) is relatively light (the mean value of δ^{18}O is −5.6‰): too light for normal meteoric waters originating from the Indian Ocean today. Light values can be achieved by two effects: either by precipitation from water that has spent considerable time over continents or high elevation (the 'continent/orographic' effect), or from prolonged very heavy rainfall (the 'amount' effect). At Sefidabeh, the first can be achieved if the rainfall originates from the Mediterranean (which

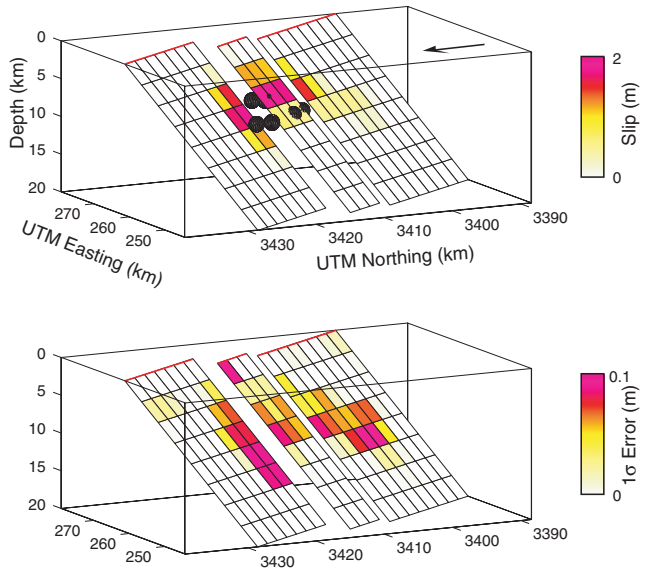

Figure 11. Perspective view of slip distribution (a) and related errors (b) for three-fault solution. The model interferogram and residual fringes calculated with this slip distribution are shown in Figs 10(c) and (d). The arrow in (a) points to North. The spheres in (a) show the locations of the earthquakes in Table 1; each sphere has a radius of 1 km.

is also isotopically lighter than the Indian Ocean anyway) in climatic conditions that are similar to those today, while the second can be achieved if the Indian monsoon reached further north than it does today, requiring local conditions that are considerably wetter. An age of 99–103 ka implies calcite formation in oxygen isotope stage (OIS) 5c. However, the age errors allow calcite formation in OIS 5e or 5a. OIS stage 5e is known to have been a pluvial event (i.e. wetter, probably monsoon influenced) in Oman (Burns *et al.* 1998, 2001). Mediterranean sapropels record pluvial episodes at 124 ka, 102 ka and 81 ka, corresponding to OIS 5e, 5c and 5a, respectively (Kroon *et al.* 1998). The petrographic evidence suggests that the carbonates were deposited in conditions of at least seasonal wetness, possibly even pluvial conditions, but anyway wetter than Sefidabeh today. This conclusion is also consistent with the stable carbon isotopes (see Appendix B3), and explains the presence of extensive alluvial fan deposits near Sefidabeh, which could not have formed under today's conditions.

5 DISCUSSION

Despite the complication of slip on multiple faults, the pattern of surface displacements in the Sefidabeh earthquakes (Fig. 6) is relatively simple, and can be explained as the elastic response to slip on buried thrust faults. In explaining the topographic structures associated with continental dip slip faults by repeated earthquakes, for example, Stein *et al.* (1988), there is generally a reasonable similarity in shape between the long-term topography and the vertical motion in a single earthquake. However, this is not the case for the Sefidabeh ridge. If we look at topographic profiles across the ridge (Fig. 13), it is a relatively short wavelength feature superimposed on a regional slope (Fig. 14). Berberian *et al.* (2000) found that near-surface faulting was dominated by slip on near vertical surfaces. The eroded saddle-like morphology resulting from the mini-graben formed due to the bedding-plane slip can be seen in some of the profiles, for example, profiles 3 and 4. The shape of the ridge primarily reflects local geological structures, combined with a regional slope inherited from earlier deformation. The Sefidabeh ridge stands up in part because it is in resistant volcanic rocks, adjacent to much weaker flysch on the southwest (Freund 1970). This relict topography obscures the cumulative deformation due to repeated earthquakes.

Nonetheless, the uplifted lake deposits give a measure of the uplift that has taken place since they were formed ∼100 Ma ago, from which we can estimate recurrence intervals for earthquakes and convergence rates on the Sefidabeh faults. We base these estimates on a picture of the development of topography and drainage inferred from geomorphological observations (Fig. 4; Berberian *et al.* 2000). Before the growth of the Sefidabeh ridge, the Butgow river appears to have drained to the northeast down the regional slope. As the NW–SE Sefidabeh ridge grew across the course of river, the river initially cut into the growing ridge; the lake deposits are found in a gorge cut into the ridge. Eventually local gradients behind the ridge were reduced sufficiently that the river began to flow around the northern end of the ridge, abandoning its original course. We assume that the lake deposits found at the base of the gorge through the Sefidabeh ridge date from that time.

The alluvial fan deposits in front of the Sefidabeh ridge could not have formed under the present arid conditions. The stable isotope measurements on the uplifted lake deposits (Section 4; Appendix B3) show that these were formed under much wetter local conditions. Unfortunately, contamination of the carbonates by

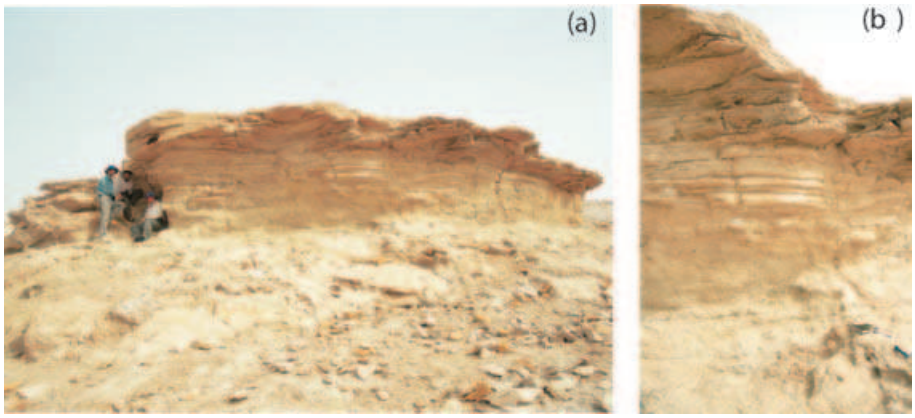

Figure 12. (a) View looking SE on the ridge above Sefidabeh village. The light-coloured rocks are the uplifted playa carbonates preserved in the now-uplifted and abandoned gorge. The bluff showing about 3 m of bedded sediments next to the people is close to the top of the exposed sedimentary sequence, which is now about 70 m above the village. (b) Close-up of the outcrop sampled in this study and described in detail in Appendix A1.

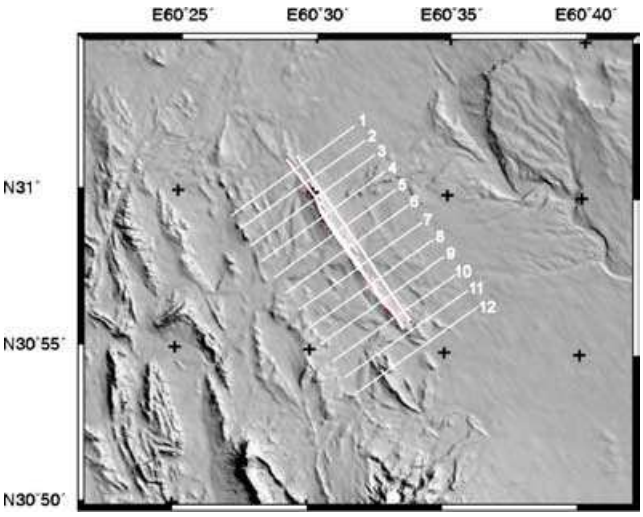

Figure 13. Location of topographic profiles across and along the Sefidabeh ridge shown in Figs 14 and 15. The profiles are drawn on a shaded relief map of the area, with illumination from an azimuth of 58° and an elevation of 40°.

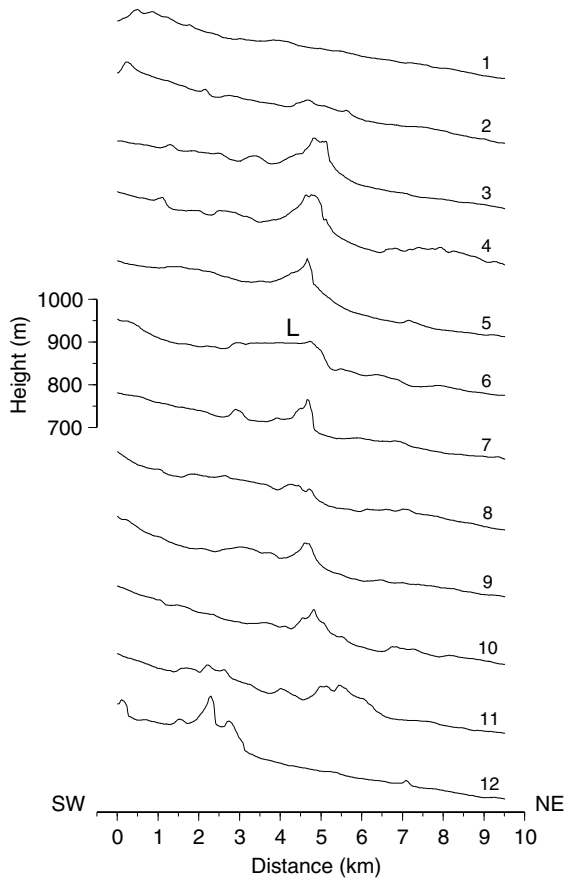

Figure 14. Topography across the Sefidabeh ridge along the lines shown in Fig. 13. The height scale-bar on the left is correctly positioned for profile 6, which crosses the uplifted lake deposits (L). Neighbouring profiles are offset vertically by the equivalent of 150 m. Profile 12 is across the Palangkuh ridge, which steps to the right (SW) of the Sefidabeh ridge.

detrital uranium and thorium cause uncertainties in age that does not allow definitive regional climatic correlation. If the Sefidabeh ridge was already a significant fraction of its present length when the lake was finally cut off, as we argue below, then much of the present deflection of the Butgow river would have occurred then. We assume that the plain in front of the Sefidabeh ridge has been modified little since that time, and that the lake deposits must then have been close to the level of the plain.

Profile 6 (Fig. 14) shows that the lake deposits are now about 70 m above the neighbouring plain. This represents the relative uplift since the lake deposits were formed; uncertainties due to the above assumptions are probably small compared to the other uncertainties discussed below. The interferogram shows that a maximum relative uplift of about 60 cm occurred in the 1994 earthquake sequence. The centre of the Sefidabeh ridge where the lake deposits are located experienced about half this maximum displacement. Assuming that 30–60 cm represents the vertical motion on the ridge in a typical event, then it would have taken 116–232 such events to uplift the lake deposits to their present height. Berberian *et al.* (2000) came to a similar estimate based on the slip expected in these earthquakes from their observed seismic moments and scaling relationships.

There is a question of what constitutes a typical earthquake sequence in this area. The modelling of the interferogram shows that for the 1994 sequence, slip only reached as far north as the lake deposits, but no further. The height of the ridge further north of the deposits shows, however, that slip must have occurred further north in the past. The InSAR modelling suggests that the earthquakes in the 1994 sequence occurred on separate closely spaced segments, with one earthquake triggering the next event on a neighbouring segment. A simple model of past events in the Sefidabeh area would be a sequence of $M_w \sim 6$ earthquakes, with the sequences differing in the number of earthquakes in the sequence and the location of the segments where slip occurred. Each $M_w \sim 6$ earthquake will produce approximately the same surface displacements around it, the total displacement at any point depending on its location relative to the individual earthquakes. The maximum displacement observed in the interferogram is likely to provide a good upper bound on the vertical motion that can occur in any sequence. In the absence of other information, we also assume that the range of uplift noted above, 30–60 cm, is a reasonable estimate of the range of uplift in past sequences.

Another uncertainty in the estimation of the number of earthquake sequences is the assumption that the total uplift associated with each event occurs solely in the earthquakes. Repeated studies have shown that coseismic surface displacements can be related to slip on the fault assuming the latter behaves as a dislocation in an elastic medium. The question is whether the region of folding above the seismically active fault behaves elastically over the long term. Certainly, if elastic stresses generated in each earthquake were to accumulate, the elastic limit would eventually be reached. Also, seismic profiling above blind thrusts in the Los Angeles area shows discrete folding concentrated into a narrow zone (Dolan *et al.* 2003). A lower limit on the number of earthquakes that have occurred can be obtained by assuming that the stresses in the near surface layers of folding relax in between earthquakes and that the slip on the fault extends directly to the surface. With peak slip of 1.5–2 m (Fig. 11), and a dip of 45° (Table 3), the maximum long-term relative vertical motion that could be produced would be about 1.2 m, and hence the number of such events required to produce the total uplift would be about 58.

Hence the estimated range for the number of events is about 60–240, that is, an estimate of 120 events with an uncertainty of a

factor of two either way. Given the age of ∼100 ka for the uplifted lake deposits, the average recurrence interval is therefore about 830 yr, again with the same level of uncertainty (420–1660 yr). Again using a peak slip on the faults of ∼1.5–2 m, and a dip of 45°, the convergence rate across the Sefidabeh faults is 1.5 mm yr^{-1} (0.7–3 mm yr^{-1}). From the known height and measured age, the average uplift rate is 0.7 mm yr^{-1}.

Berberian *et al.* (2000) also considered how the Sefidabeh thrust might have grown in length. They used a result of Cowie & Scholz (1992a) for the number of earthquakes N required to increase the length of a fault from an initial value L_0 to a length L:

$$N = \frac{\log L/L_0}{\log(1+\alpha/\gamma)},$$

where α is the ratio of mean slip during an earthquake to the fault length, and γ is the ratio of mean accumulated displacement on a fault to its length. The ratio $r = \alpha/\gamma$ represents the proportional increase in fault length during each earthquake. Estimating that $L/L_0 \sim 1.9$, and using a value of $r = \sim 1.5 \times 10^{-3}$, they concluded that about 430 earthquakes were required, rather more than the number of earthquakes required to uplift the lake deposits.

If a fault increases in length by the same proportion of its length in each earthquake throughout its history, and the slip that occurs in each earthquake is proportional to the length, then the cumulative offset on the fault would be expected to vary smoothly along its length from a maximum at its centre (e.g. Cowie & Scholz 1992b). However, if we examine a topographic profile along the length of the Sefidabeh ridge (Fig. 15), a somewhat different picture emerges. The cumulative offset, as measured by the height of the ridge above the plain at its foot, is roughly constant between distances of 2.6 and 8.2 km along the profile, falling off rapidly at its edges. This is suggestive of an alternative picture of fault growth, in which there are initially many small faults that rapidly coalesce to form a single longer fault, such that subsequently the slip in each earthquake and hence the cumulative offset is approximately constant along this initial length (e.g. Cowie 1998). Hence, at the time the lake was abandoned and the river Butgow was deflected by the growing ridge, it may well have already extended about 4 km north of the lake deposits. If we assume that $L_0 = 5.6$ km, that is, the segment of roughly constant height above the plain, and that the river always flows around the northern end of the growing ridge, then a better estimate of L/L_0 is 1.3. From eq. (5), this leads to a new estimate of 175 for the number of earthquakes required, well within the range estimated from the amount of uplift, even without allowing for uncertainties in the value of r. If the ridge has propagated 2 km in 115–230 earthquakes, then the increase in length per earthquake has been 8.7–17.4 m, with an average propagation rate of 2 cm yr^{-1}.

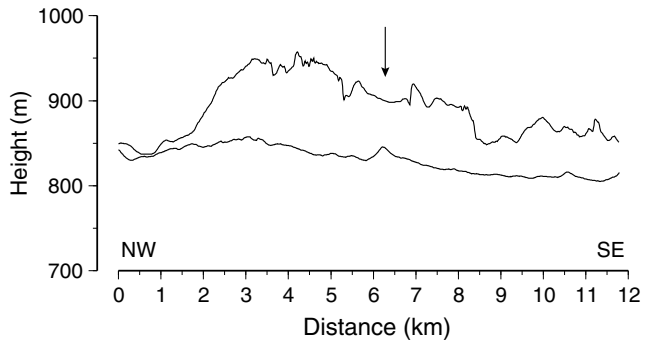

Figure 15. Topographic profiles along the crest of the Sefidabeh ridge and parallel to the ridge across the plain at its foot. Locations of the profiles are shown in Fig. 13. The arrow marks the location of the uplifted lake deposits.

Apart from quantifying and locating the slip in the 1994 earthquakes, and providing evidence of timing and hence deformation rates, this study has one more significant contribution to make. It confirms the suggestion, implicit in Berberian *et al.* (2000), that we can correctly interpret the evidence in the landscape for active, blind thrust faulting. In the case of Sefidabeh, even though the coseismic deformation resembles folding, the overall topography does not (Figs 3 and 14) because of inherited earlier deformation. Nonetheless, the pattern of deformation due to current activity is unmistakeable, in the form of recent changes in drainage incision and deflection. This is a significant lesson in what to look for in those places where active folds do not necessarily resemble folds in their surface shape and the topography as does happen in simpler places (e.g. Keller *et al.* 1998; Jackson *et al.* 1996).

ACKNOWLEDGMENTS

This research has been supported by the Natural Environment Research Council through the Centre for the Observation and Modelling of Earthquakes and Tectonics (COMET), as well as a research fellowship to TW. ERS SAR data was provided by the European Space Agency under project AOE-621. We are grateful to JPL/Caltech for the use of the ROI_pac software. We thank Sarah Dennis for preparation of samples for U-series dating and stable isotope analysis.

REFERENCES

Bayasgalan, A., Jackson, J., Ritz, J.-F. & Cartier, S., 1999. Field examples of strike-slip fault terminations in Mongolia and their tectonic significance, *Tectonics,* **18,** 394–411.

Berberian, M, Jackson, J.A., Qorashi, M., Talebian, M., Khatib, M. & Priestley, K., 2000. The 1994 Sefidabeh earthquakes in eastern Iran: blind thrusting and bedding plane slip on a growing anticline, and active tectonics of the Sistan suture zone, *Geophys. J. Int.,* **142,** 283–299.

Bischoff, J.L. & Fitzpatrick, J.A., 1991. U-series dating of impure carbonates: an isochron technique using total-sample dissolution, *Geochimica Cosmochimica Acta,* **55,** 543–554.

Bondar, I., Myers, S.C., Engdahl, E.R. & Bergman, E.A., 2004. Epicentre accuracy based on seismic network criteria, *Geophys. J. Int.,* **156,** 1–14, doi: 10.1046/j.1365-246X.2004.02070.x

Bro, R. & De Jong, S., 1997. A fast non-negativity-constrained least squares algorithm, *J. Chemometrics,* **11,** 392–401.

Burns, S.J., Matter, A., Frank, N. & Mangini, A., 1998. Speleothem-based paleoclimate record from northern Oman, *Geology,* **26,** 499–502.

Burns, S.J., Fleitmann, D., Matter, A., Neff, U. & Mangini, A., 2001. Speleothem evidence from Oman for continental pluvial events during interglacial periods, *Geology,* **29,** 623–626.

Chu, D. & Gordon, R.G., 1998. Current plate motions across the Red Sea, *Geophys. J. Int.,* **135,** 313–328.

Coplen, T.B., 1994. Reporting of stable hydrogen, carbon and oxygen isotopic abundances, *Pure & Applied Chemistry,* **66,** 273–276.

Cowie, P.A., 1998. A healing-reloading feedback control on the growth rate of seismogenic faults, *J. Struct. Geol.,* **20,** 1075–1087.

Cowie, P.A. & Scholz, C.H., 1992a. Growth of faults by accumulation of seismic slip, *J. geophys. Res.,* **97,** 11 085–11 095.

Cowie, P.A. & Scholz, C.H., 1992b. Physical explanation for the displacement-length relationship of faults using a post-yeild fracture mechanics model, *J. Struct. Geol.,* **14,** 1133–1148.

DeMets, C., Gordon, R.G., Argus, D.F. & Stein, S., 1994. Effect of recent revisions to the geomagnetic reversal time scale on estimates of current plate motions, *Geophys. Res. Lett.,* **21,** 2191–2194.

Dickson, J.A.D., 1965. A modified staining technique for carbonates in thin section, *Nature,* **205,** 587.

Dolan, J.F., Christofferson, S.A. & Shaw, J.H., 2003. Recognition of paleoearthquakes on the Puente Hills blind thrust fault, California, *Science,* **300,** 115–118.

Engdahl, E.R., van der Hilst, R. & Buland, R., 1998. Global teleseismic earthquake relocation with improved travel times and procedures for depth determination, *Bull. seism. Soc. Am.,* **88,** 722–743.

Farr, T. & Kobrich, M., 2000. Shuttle radar topographic mission produces a wealth of data, *EOS, Trans. Am. geophys. Un.,* **81,** 583-585.

Ferguson, J., Burne, R.V. & Chambers, L.A., 1982. Lithification of peritidal carbonates by continental brines at Fisherman Bay, south Australia, to form a megopolygon/spelean limestone association, *Journal of Sedimentary Petrology,* **52,** 1127–1147.

Freund, R., 1970. Rotation of strike-slip faults in Sistan, southeast Iran, *J. Geol,* **78,** 188-200.

Hanssen, R.F., 2001, *Radar Interferometry: Data Interpretation and Error Analysis*, 308pp., Kluwer Academic Publishers: Netherlands.

Hays, P.D. & Grossman, E.L., 1991. Oxygen isotopes in meteoric calcite cements as indicators of continental palaeoclimate, *Geology,* **19,** 441–444.

Ivanovich, M. & Harmon, R.S., 1992, *Uranium Series Disequilibrium: Application to Environmental Problems in the Earth Sciences*, 910 pp., Clarendon Press, Oxford.

Jackson, J.A., Norris, R. & Youngson, J., 1996. The structural development of active fault and fold systems in central Otago, New Zealand: evidence revealed by drainage patterns, *J. Struct. Geol.,* **18,** 217–234.

Jónsson, S., Zebker, H., Segall, P. & Amelung, F., 2002. Fault slip distribution of the 1999 M_w 7.1 Hector Mine, California, earthquake, estimated from satellite radar and GPS measurements, *Bull. seism. Soc. Am.,* **92,** 1377–1389.

Jordan, T.H. & Sverdrup, K.A., 1981. Teleseismic location techniques and their application to earthquake clusters in the south-central Pacific, *Bull. seism. Soc. Am.,* **71,** 1105–1130.

Kaufman, A., 1993. An evaluation of several methods for determining ^{230}Th/U ages in impure carbonates, *Geochimica Cosmochimica Acta,* **57,** 2303–2317.

Kaufmann, A. & Broecker, W.S., 1965. Comparison of ^{230}Th and ^{14}C ages for carbonate materials from Lakes Lahontan and Bonneville. *J. geophys. Res.,* **70,** 4039–4054.

Keller, E.A., Zepeda, R.L., Rockwell, T.K., Ku, T.L. & Dinklage, W.S., 1998. Active tectonics at Wheeler Ridge, southern San Joaquin Valley, California, *Geol. Soc. Am. Bull.,* **110,** 298–310.

Kroon, D., Alexander, I., Little, M., Lourens, L.J., Mathewson, A., Robertson, A.H. F. & Sakamoto, T., 1998. Oxygen isotope and sapropel stratigraphy in the Eastern Mediterranean during the last 3.2 million years, in *Proceedings of the Ocean Drilling Program, Scientific Results*, Vol. 160, pp. 181–189, eds Robertson, A.H.F., Emeis, K.-C., Richter, C. & Camerlenghi, A.

Ku, T.-L. & Liang, Z.-C., 1984. The dating of impure carbonates with decay-series isotopes. *Nucl. Instr. Meth. Phys. Res.,* **223,** 563–571.

Ludwig, K.R., 2001. Isoplot/Ex, version 2.49: a geochronological toolkit for Microsoft Excel, *Berkeley Geochronological Center Special Publication,* 1a, 56 pp.

Ludwig, K.R., 2003. Mathematical-statistical treatment of data and errors for ^{230}Th/U geochronology, *Uranium Series Geochemistry, Reviews in Mineralogy and Geochemistry*,Vol. 52, p. 656, in Bourdon, B., Henderson, G.M., Lundstrom, C.C. & Turner, S.P., Mineralogical Society of America.

Ludwig, K.R. & Titterington, D.M., 1994. Calculation of ^{230}Th/U isochrons, ages, and errors, *Geochimica et Cosmochimica Acta,* **58,** 5031–5042.

Luo, S. & Ku, T.L., 1991. U-series isochron dating: a generalized method employing total sample dissolution, *Geochimica Cosmochimica Acta,* **55,** 555–564.

Massonnet, D. & Feigl, K.L., 1998. Radar interferometry and its application to changes in the earth's surface, *Rev. Geophys.,* **36,** 441–500.

Menke, W., 1989. *Geophysical Data Analysis: Discrete Inverse Theory*. Revised edn, Academic Press Inc., Harcourt Brace Jovanovich Publishers, San Deigo.

Okada, Y., 1985. Surface deformation due to shear and tensile faults in a half-space, *Bull. seism. Soc. Am.,* **75,** 1135–1154.

Ritzwoller, M.H., Shapiro, N.M., Levshin, A.L., Bergman, E.A. & Engdahl, E.R., 2003. Ability of a global three-dimensional model to locate regional events, *J. geophys. Res.,* **108,** 2353, doi:10.1029/2002JB002167.

Rosen, P.A., Hensley, S., Peltzer, G. & Simons, M., 2004. Updated Repeat Orbit Interferometry package released, *EOS, Trans. Am. geophys. Un.,* **85,** 35.

Rozanski, K., Araguas-Araguas, L. & Gonfiantini, R., 1993. Isotopic patterns in modern global precipitation, in *Climate change in continental isotopic records*, pp. 1–36, eds Swart, P.K., Lohmann, K.C., McKenzie, J. & Savin, S., American Geophysical Union, Geophysical Monograph 78, Washington DC.

Rubinstein, R.Y., 1981. *Simulation and the Monte Carlo Method*, Wiley series in probability and mathematical statistics, Wiley New York.

Schwarcz, H.P., 1989. Uranium series dating, *Quat. Int.,* **1,** 7–17.

Schwarcz, H.P. & Latham, A.G., 1989. Dirty calcites: 1. Uranium-series dating of contaminated calcite using leachates alone, *Chemical Geology,* **80,** 35–43.

Sella, G.F., Dixon, T.H. & Mao, A., 2002. REVEL: A model for recent plate velocities from space geodesy, *J. geophys. Res.,* **107,** 10.1029/2000JB000033.

Singhvi, A.K., Banerjee, D., Ramesh, R., Rajaguru, S.N. & Gogte, V., 1996. A luminescence method for dating 'dirty' pedogenic carbonates for paleoenvironmental reconstruction, *Earth planet. Sci. Lett.,* **139,** 321–332.

Stein, R.S., King, G.C.P. & Rundle, J.B., 1988. The growth of geological structures by repeated earthquakes: 2. Field examples of continental dip-slip faults, *J. geophys. Res.,* **93,** 13 319–13 311.

Vernant, Ph.*et al*., 2004. Present-day crustal deformation and plate kinematics in the Middle East constrained by GPS measurements in Iran and northern Oman, *Geophys. J. Int.,* **157,** 381–398.

Walker, R. & Jackson, J., 2002. Offset and evolution of the Gowk fault, S.E. Iran: a major intra-continental strike-slip system, *J. Struct. Geol.,* **24,** 1677–1698.

Walker, R. & Jackson, J., 2004. Active tectonics and late Tertiary strain distribution in central and eastern Iran, *Tectonics,* TC5010, doi:10.1029/2003TC001529.

Wright, T.J., Parsons, B.E., Jackson, J.A., Haynes, M., Fielding, E.J., England, P.C. & Clarke, P.J., 1999. Source parameters of the 1 October 1995 Dinar (Turkey) earthquake from SAR interferometry and seismic bodywave modelling, *Earth planet. Sci. Lett.,* **172,** 23–37.

Wright, T.J., Lu, Z. & Wicks, C., 2004. Constraining the slip distribution and fault geometry of the M_w 7.9, 3 November 2002, Denali Fault earthquake with interferometric Synthetic Aperture Radar and Global Positioning System data, *Bull. seism. Soc. Am.,* **94,** S175–S189.

Yurtsever, Y. 1975, *Worldwide survey of stable isotopes in precipitation: Reports section isotope hydrology*. International Atomic Energy Agency, p. 40.

APPENDIX A: InSAR ERROR ANALYSIS

To determine parameter errors for our non-linear inversions, we followed the method of Wright *et al.* (in preparation), who use the Monte Carlo simulation of correlated noise. This method accounts for the spatial correlations in the atmospheric and orbital components of InSAR noise. It has three stages:

(1) analysis of InSAR noise;
(2) simulation of noisy data sets and
(3) inversion of noisy data sets to determine uncertainties in model parameters.

We first determined a best-fit 1-D covariance function, for example, Hanssen (2001), that approximates the noise in coseismic interferogram by analysing a ∼50 by 50 km region in the northwest of the image, where no significant coseismic displacements occurred.

The 1-D covariance function is the radial average of the interferogram's 2-D autocovariance function—the cosine Fourier transform of the power spectrum (e.g. Hanssen 2001). We find that a simple exponential function

$$C(r) = \sigma^2 \mathrm{e}^{-\alpha r} \tag{A1}$$

provides a good approximation to the observed covariance function, where σ^2 is the variance, r is the separation of the observations in kilometres and α determines the e-folding correlation length scale. In this case, σ was $\sim$5 mm, and α was $\sim$0.015, equivalent to a length scale of $\sim$7 km.

To simulate the correlated noise, we first constructed a full variance–covariance matrix, $\mathbf{\Sigma}$, for our sampled data points, assuming that the noise structure was isotropic and identical throughout the image. A vector of spatially correlated noise, $\mathbf{y}$, can then be calculated from a vector of Guassian, uncorrelated noise, $\mathbf{x}$, with a mean of zero and a standard deviation of 1, by

$$\mathbf{y} = \mathbf{L}\mathbf{x}, \tag{A2}$$

where $\mathbf{L}$ is the Cholesky decomposition of the variance-covariance matrix, $\Sigma = \mathbf{L}\mathbf{L}^{\mathrm{T}}$, (Rubinstein 1981). The correlated noise is then added back to the original data vector to give a new noisy data set. We repeated this procedure 100 times to provide an ensemble of noisy data sets.

Each of these noisy data sets is then used in the appropriate inversion procedure to give a set of model parameters. The distribution of these model parameter gives their error. One advantage of this method is that it also enables us to determine the trade-offs between different model parameters. An example is given in Fig. A1 for our single fault inversion, where we have plotted every parameter against every other parameter for the 100 different inversion results. Several strong trade-offs are evident, such as between

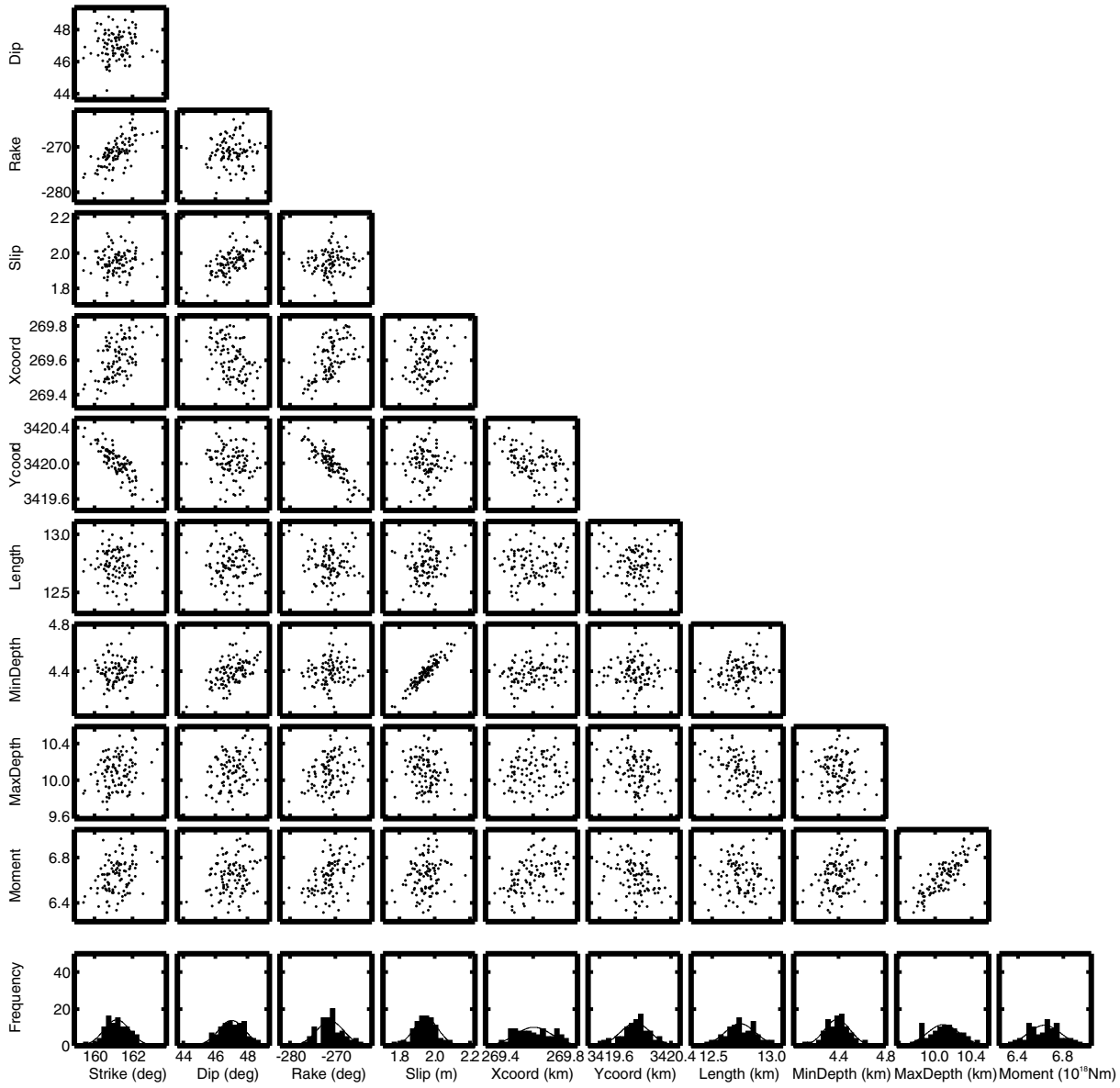

Figure A1. Model parameter trade-offs for uniform-slip model. Each of the 100 dots in each of the upper plots is the best-fit solution for one data set to which Monte Carlo, correlated noise has been added. Histograms summarize the results for each parameter.

slip and the minimum depth of faulting, and between rake and *y*-coordinate.

APPENDIX B: ANALYSIS OF THE SEFIDABEH CARBONATES

B1 Petrographic description

Fabric descriptions are based on hand specimens and stained (Dickson 1965) thin-section information. Cathodoluminescence (CL) analysis of thin sections was done using a cold cathode Technosyn instrument run at accelerating voltage of 18–20 kV and a gun current of 180–200 μA.

The deposit comprises a basal 3.0 m of fine-medium calcite cemented sandstone passing upward into 2.10 m of progressively better cemented sandy limestone, superficially resembling travertine. The basal sandy unit contains angular breccia fragments and blocks of bedded sandy limestone. Bedding and degree of calcite cementation become progressively more pronounced upward in the upper unit, resulting in 0.70-m-thick cap of tightly cemented limestone at the top of the deposit. The better-cemented limestones taste salty and contain abundant millimetre-sized, irregular vugs that crudely follow bedding. Botryoidal calcite cement lines the walls of many of these vugs.

Thin sections show these limestones to be composed of non-ferroan micrites and microspars with variable amounts of sandy detritus. The detritus is mainly composed of quartz and feldspar, although CL shows that 2–5 per cent of the sand grains are reworked basement limestone clasts. Ostracod carapaces are the only fossil remains and these are rare. The micrites contain clotted, wispy and cellular fabrics which are probably of microbial origin. In places peloidal or ped-like micritic fabrics are common, associated with patchy accumulations of microspar. Botryoidal non-ferroan radial calcite cement lines the walls of many of the vugs, and some have dripstone fabrics. Smaller former open spaces are partially or wholly infilled by non-ferroan sparry calcite cement. The vugs were probably formed by upward-flowing groundwater that ruptured cemented crusts (*cf.* Ferguson *et al.* 1982), although some may have contained evaporite salts.

B2 U-series dating

Dating method

We used the leachate (L/L) method of analysing contaminated carbonates (Schwarcz & Latham 1989). Seven samples were dissolved in ^{229}Th/^{236}U-spiked dilute HNO_3 ($\leq$2 M with the exception of one sample which was leached in 5 M), for a standard time. After filtering and concentration of U and Th on $FeOH_3$, U and Th were separated and purified on anion exchange columns in the nitric form, electroplated onto stainless steel discs from an ammonium sulphate solution and alpha counted.

Results are shown in Table B1 and plotted in isotope ratio space in Figures B1 and B2. The U-series age equation may be written as:

$$^{230}\mathrm{Th}/^{234}\mathrm{U} = (^{238}\mathrm{U}/^{234}\mathrm{U})[1 - \exp(-\lambda_0 t)] + [\lambda_0/(\lambda_0 - \lambda_4)](1 - {}^{238}\mathrm{U}/^{234}\mathrm{U})[1 - \exp(\lambda_4 - \lambda_0)t],$$

where λ_0 and λ_4 are the decay constants for ^{230}Th and ^{234}U, respectively, and t is the age, determined iteratively (Kaufmann & Broecker 1965).

Table B1. U-series isotope ratios for Sefidabeh S7 calcite cement samples. Errors shown are 1 standard deviation counting statistics.

Lab No	U (ppm)	^{234}U/^{232}Th	^{238}U/^{232}Th	^{230}Th/^{232}Th
UEA802	0.47	10.701 ± 0.789	6.383 ± 0.473	11.514 ± 0.660
UEA810	0.40	8.237 ± 0.436	4.867 ± 0.265	11.346 ± 0.508
UEA811	0.46	12.621 ± 0.749	7.345 ± 0.444	14.202 ± 0.702
UEA879	0.53	11.404 ± 0.752	6.485 ± 0.447	13.565 ± 0.681
UEA880	0.58	10.716 ± 0.699	6.278 ± 0.418	12.430 ± 0.697
UEA881	0.39	9.214 ± 0.833	5.557 ± 0.513	12.132 ± 1.001
UEA882	0.47	10.775 ± 0.690	5.865 ± 0.388	10.406 ± 0.567

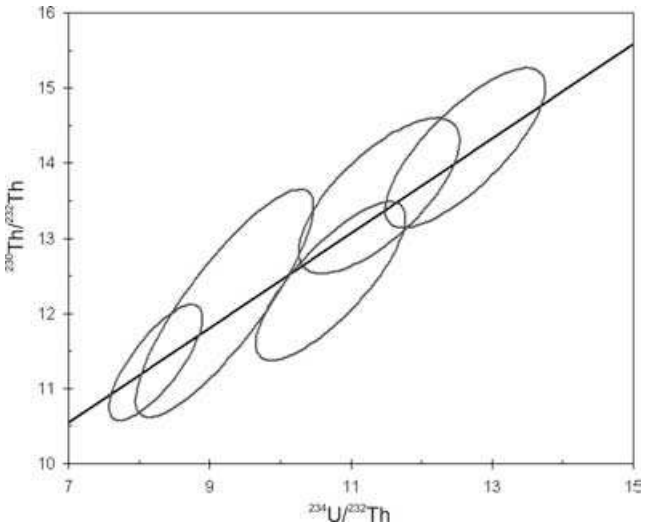

Figure B1. Isotope data plotted as ^{230}Th/^{232}Th vs. ^{234}U/^{232}Th. The slope of the line gives the authigenic ^{230}Th/^{234}U composition of the carbonate (0.63).

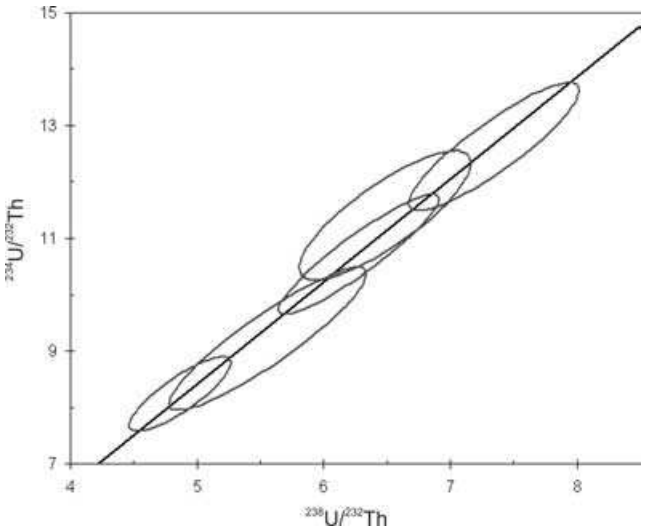

Figure B2. Isotope data plotted as ^{234}U/^{232}Th vs. ^{238}U/^{232}Th. The slope of the line gives the authigenic ^{234}U/^{238}U composition of the carbonate (1.83).

Results

The isotope ratios ^{230}Th/^{234}U and ^{234}U/^{238}U are directly given by the slopes of the best-fit lines in the plotted coordinates chosen here. The isotope pair data for one particular sample, UEA882, generate a point which, on the ^{230}Th/^{232}Th versus ^{234}U/^{232}Th diagram, lies more than three standard deviations from the best-fit regression line,

Table B2. Age data derived from isochron plots. Six-point plots exclude sample 882 only. Five-point plots exclude UEA882 and UEA802. MSWD (mean square of weighted deviates) values indicate how closely the observed data scatter matches the scatter predicted from the errors and error correlations of the data points. P = probability of fit. Errors are 1 standard deviation. *Robust regression; ** model 1 regression (Ludwig 2001).

	$^{230}Th/^{234}U$	MSWD	P	$^{234}U/^{238}U$	MSWD	P	Age (ka)
Six points*	$0.65^{+0.37}_{-0.30}$	—	—	1.82 ± 0.17	0.25	0.86	103^{+164}_{-57}
Five points**	0.63 ± 0.11	0.51	0.68	1.82 ± 0.17	0.25	0.86	99^{+30}_{-24}

Table B3. Stable isotope data for Sefidabeh carbonates.

Sample no.	$\delta^{13}C$	$\delta^{18}O$	Material sampled
S7	−7.15	−5.70	Clotted micritic fenestral fabrics with Three stages of early diagenetic cements
S6	−7.03	−5.64	Clotted micritic fenestral fabrics with Some early diagenetic cementation
S5	−7.05	−5.74	Clotted micritic fabrics
S3	−7.20	−5.41	Clotted micritic fabric
Mean	−7.11	−5.62	

and on the $^{234}U/^{232}Th$ versus $^{238}U/^{232}Th$ diagram a point, which is unique in lying more than one standard deviation from the line. Either the more concentrated acid leach applied to this sample (see above) preferentially solubilized both uranium isotopes relative to thorium, or the detritus in this subsample may possess a different isotopic composition to the others. This sample has been omitted from the isochron diagrams. The same is probably true of the anomalous sample referred to in the main text, UEA802, to a lesser degree. Ages have been derived from both a five-data-point plot (Figs B1 and B2), excluding both 802 and 882, and a six-data-point plot, retaining 802. Table B2 summarizes the dating information drawn from the isochrons.

B3 Stable isotopes

Subsamples of 2–5 mg for stable isotope analysis were drilled from slabbed and polished hand specimens. Organic matter was removed by low temperature plasma ashing and the samples were then processed using normal laboratory procedures and measured on a VG Sira Series II mass spectrometer calibrated using the NBS 18 and NBS 19 standards. Isotopic data are reported in delta notation relative to the Vienna Pee Dee Belemnite (VPDB) international scale (Coplen 1994). Precision for the laboratory standard and duplicates at UEA was in both cases better than $\pm 2\sigma$ 0.06‰ for $\delta^{13}C$ and $\pm 2\sigma$ 0.10‰ for $\delta^{18}O$. Measurements on four of the Sefidabeh samples are given in Table B3.

The mean $\delta^{18}O$ value for the calcite precipitate is −5.6‰ VPDB, with little variance between samples. Assuming equilibrium fractionation and temperatures of calcite formation in the range 20–30°C, these calcite $\delta^{18}O$ values correspond to water $\delta^{18}O$ values of between −4.7 and −2.6‰ VSMOW (Vienna Standard Mean Ocean Water), using the Hays & Grossman (1991) equation.

Given that there are multiple generations of cementation in these calcretes the isotopic data will be recording an average value of micrite and various microspars and sparry calcite cements. Although the latter are of small mass they cannot be ignored totally, and may affect the bulk isotopic composition a little (probably resulting in slightly more negative $\delta^{18}O$ value than in pure micrite).

Modern average $\delta^{18}O$ for rainfall at the latitude of central Iran is expected to be in the range −2 to −4‰ VSMOW (Yurtsever 1975), although in continental settings this will be modified toward lighter values by both continentality (i.e. prolonged moisture transport over land) and orographic (altitude) effects. Thus the weighted mean value at Tehran is −6.3‰ VSMOW and at Kabul is −7.1‰ VSMOW, both of which are relatively higher and further inland. By contrast, the weighted mean at Bahrain, in the Persian Gulf, is −0.9‰ VSMOW (all from Rozanski *et al.* 1993).

If the waters that precipitated the calcites had not evaporated much they might indicate equilibrium with meteoric waters with $\delta^{18}O$ values similar to today. However, the association of evaporite salts and calcite cementation point to at least seasonal aridity, suggesting that the waters that precipitated the calcites would have been evaporated somewhat. This being so, the isotopic composition of recharge would be more negative than −2.5‰ VSMOW (minimum) and probably more negative than −5.0‰ VSMOW. Air masses originating from the south or southwest of the study site would be maritime oceanic and too isotopically enriched to be the source of recharge. This argument suggests that air masses that sourced recharge came from the west or northwest and had significant continental/orographic effects that resulted in rainfall with isotopically light $\delta^{18}O$.

However, there is also evidence from Oman that the Indian Ocean monsoon system moved further north in the past (during OIS 5a, 5e, 7a and 9 Burns *et al.* 1998, 2001). Large negative $\delta^{18}O$ values of recharge in the Sefidabeh region could therefore also be due to rainout effects caused by monsoon rainfall, providing an alternative explanation to that given above. Thus, while the precision on the age of the deposit is not critical for an estimate of fault growth rates, it is important for the palaeoclimatic interpretation. An age of 99–103 ka implies calcite formation in OIS 5c where the Oman record shows no evidence of wetter climate. However, the errors allow calcite formation in OIS 5e or 5a, monsoon influenced pluvials in Oman (Burns *et al.* 1998, 2001).

The $\delta^{18}O$ values taken alone are not diagnostic for choosing between the two climatic scenarios, that is, rainfall with strong continentality/orographic effects or rainfall with strong amount effects (monsoonal). The mean $\delta^{13}C$ value of −7.1‰ VPDB suggests a significant component of soil carbon incorporation in the calcite. The negative value also suggests that CO_2 degassing at the springs was not vigorous enough to have fractionated the carbon isotopes (*cf.* Ferguson *et al.* 1982). Calcrete $\delta^{13}C$ values of −7 to −8.6‰ VPDB in 5–19 ka Thar desert pedogenic calcretes have been taken to indicate wet climatic conditions (Singhvi *et al.* 1996).